Bacterial-Derived, Compressible, and Hierarchical Porous Carbon for High-Performance Potassium-Ion Batteries
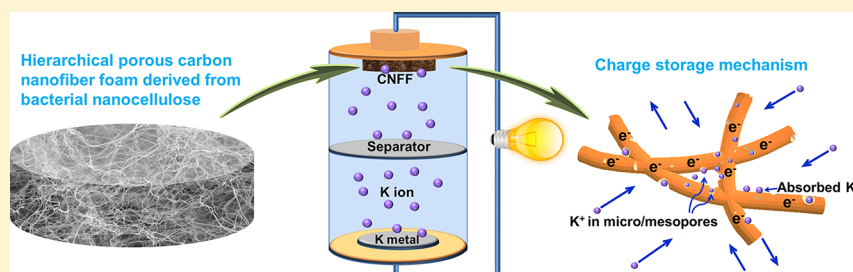
Hongyan Li,[†,#] Zheng Cheng,[†,#] Qing Zhang,[†] Avi Natan,[†] Yang Yang,[†] Daxian Cao,[†] and Hongli Zhu*,[†]

[†]Department of Mechanical and Industrial Engineering, Northeastern University, Boston, Massachusetts 02115, United States

S *Supporting Information*

ABSTRACT: Hierarchical-structured electrodes having merits of superior cycling stability and high rate performance are highly desired for next-generation energy storage. For the first time, we reported a compressible and hierarchical porous carbon nanofiber foam (CNFF) derived from a sustainable and abundant biomaterial resource, bacterial cellulose, for boosting the electrochemical performance of potassium-ion batteries. The CNFF free-standing electrode with a hierarchical porous three-dimensional structure demonstrated excellent rate performance and outstanding cyclic stability in the extended cycling test. Specifically, in the long-term cycling-stability test, the CNFF electrode maintained a stable capacity of 158 mA h g^{-1} after 2000 cycles at a high current density of 1000 mA g^{-1}, which has an average capacity decay of 0.006% per cycle. After that, the CNFF electrode maintained a capacity of 141 mA h g^{-1} at a current density of 2000 mA g^{-1} for another 1500 cycles, and a capacity of 122 mA h g^{-1} at a current density of 5000 mA g^{-1} for an additional 1000 cycles. The mechanism for the outstanding performance is that the hierarchical porous and stable CNFF with high surface area and high electronic conductivity provides sufficient sites for potassium-ion storage. Furthermore, quantitative kinetics analysis has validated the capacitive- and diffusion-controlled charge-storage contributions in the carbon-foam electrode. This work will inspire the search for cost-effective and sustainable materials for potassium electrochemical energy storage.

KEYWORDS: Potassium-ion batteries, bacterial cellulose, carbon nanofiber, hierarchical porous structure, compressible carbon foam

Lithium-based batteries are attractive energy sources because of the high energy density and low standard reduction potential of lithium metal. However, the application of lithium batteries is limited by the scarcity of lithium in the Earth's crust, only 20 ppm.[1,2] In comparison, potassium, at 17 000 ppm, is much more abundant; therefore, potassium-based batteries are more affordable than their lithium counterparts. Extensive research efforts on the development of potassium-ion batteries for large-scale energy storage have been carried out since 2015.[3,4] In the past 2 years, several potassium-ion batteries (PIBs) anode materials such as graphite,[5,6] hard carbon microspheres,[7] Prussian blue,[8] MXene,[9] Sn–C composite,[10] chitin-based hard carbon,[11] and transition-metal compounds[12] have been studied. The main challenge facing PIBs is the low intrinsic kinetic of intercalation reaction caused by the large size of potassium ions (1.38 Å) compared with lithium ions (0.76 Å) and sodium ions (1.02 Å). This larger ion size results in low reversible capacity and poor cycling stability.[13] For this reason, pursuing highly ion-accessible PIBs anode materials with good structural stability is the key to improving the overall electrochemical performance of these batteries.
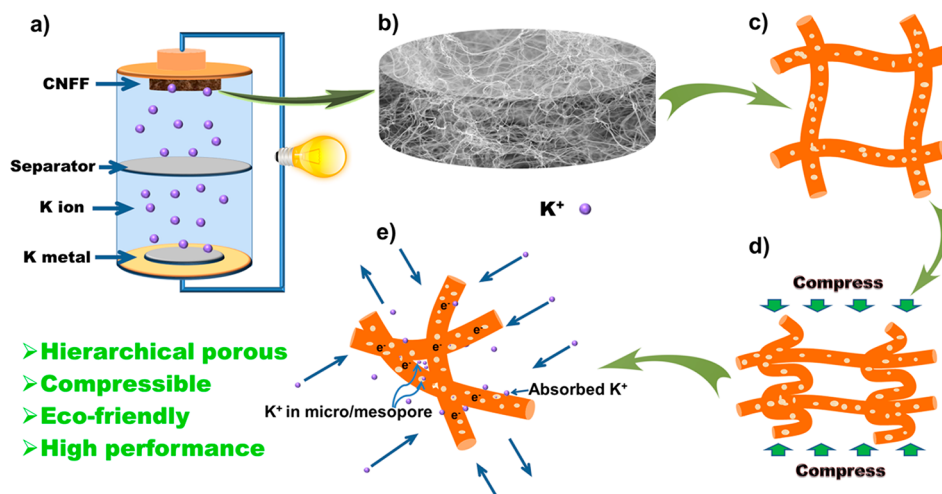
Carbonaceous materials are very attractive for PIB anodes due to their high conductivity and chemical stability. For instance, Ci et al. reported FeCl$_3$-intercalated graphite as an anode of PIBs.[14] Yang et al. reported sulfur and oxygen co-doped porous hard carbon microspheres for PIBs.[15] Du et al. also used spheroid-like KTi$_2$(PO$_4$)$_3$@C nanocomposites as anode material for PIBs.[16] However, considering the small-scale synthesis procedures for these works, the large-scale application of carbon-based anodes in PIBs remains challenging. Therefore, biomaterial resources are being researched as alternatives because they are sustainable and abundant. Bacterial cellulose (BC) nanofibers can be sustainably synthesized by bacteria culture on a large scale. The BC contain ultrafine nanofibrillar reticulated structures.[17] BC

Scheme 1. Schematic Diagrams of Electrodes[a]

[a](a) Schematic diagram of assembling CNFF freestanding electrode into a potassium-ion half-cell with a potassium metal counter electrode. (b) Schematic diagram of potassium-ion storage in CNFF surface structure. (c, d) Schematic of the CNFF electrode's high compressibility. (e) Schematic of electron transfer and potassium ions storage in CNFF electrode.
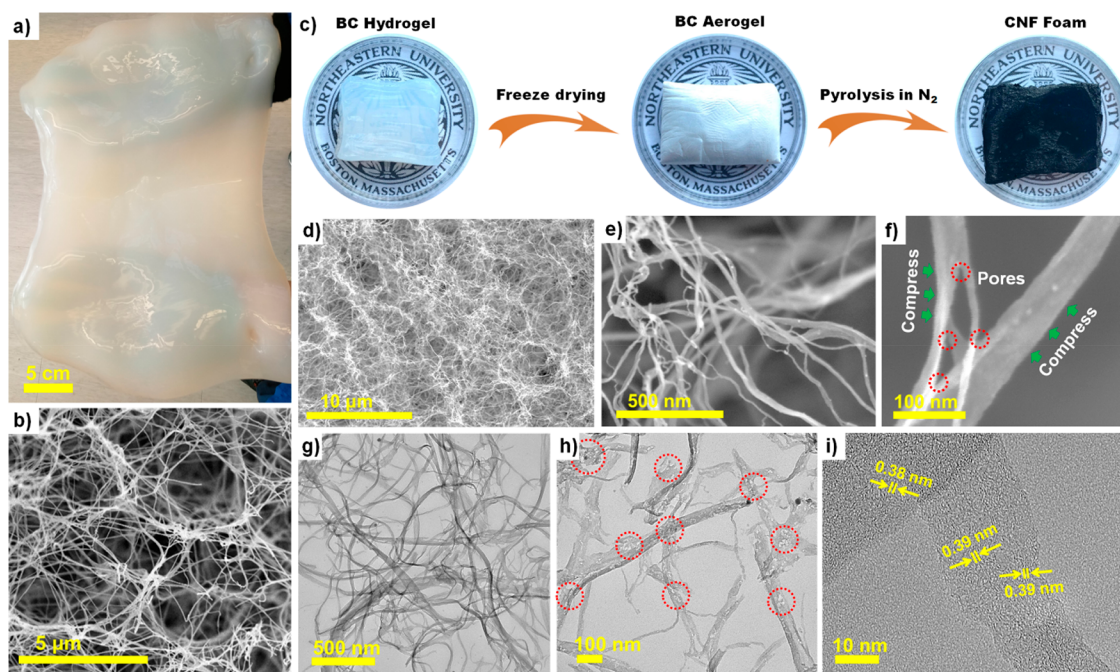

Figure 1. (a) Large piece of purified BC hydrogel with fiber content of ∼0.5 wt% are generated by a cost-effective *Acetobacter xylinum* fermentation process in a large scale. (b) SEM images of original BC aerogel. (c) Schematic diagram of preparation of CNFF. (d) SEM image of CNFF, showing a porous and 3D network structure. (e) High-magnification SEM image of CNFF. (f) High-magnification SEM image of carbon nanofibers. (g) TEM image of CNFF. (h) High-magnification TEM image of CNFF with red dotted circle in panel h showing the porous structure. (i) HR-TEM image of CNFF. (The Northeastern University seal is reproduced with permission.).

possesses high purity (70−90%),[18,19] high crystallinity (84−89%),[19,20] excellent mechanical properties (490 MPa tensile strength and 17.6 GPa Young's modulus),[19,21] and good biodegradability and biocompatibility, which render BC an appealing material for a wide range of applications such as the food and textile industries, biomedical fields, etc.[22,23]

Herein, carbon nanofiber foam (CNFF) was obtained through the pyrolysis of the BC. The resulting CNFF has a three-dimensional (3D) network with hierarchical micro- and mesopores structures and a high Brunauer−Emmett−Teller (BET) surface area (778.75 m^2 g^{-1}). Meanwhile, for the first time, such compressible CNFF has been used as freestanding anode for PIBs, and it exhibits excellent rate performance and ultralong cycling stability. The prepared CNFF was tested in a PIBs half-cell with the potassium metal as the counter electrode (Scheme 1a,b). As illustrated in Scheme 1c,d, the CNFF electrode presents high compressibility. The 3D networking structure is beneficial for ion transportation during the depotassiation and potassiation processes of the battery (Scheme 1e). Additionally, the highly reversible capacity and ultralong cycle life of PIBs are attributed to the unique structure of CNFF (Scheme 1e). The first aspect of the
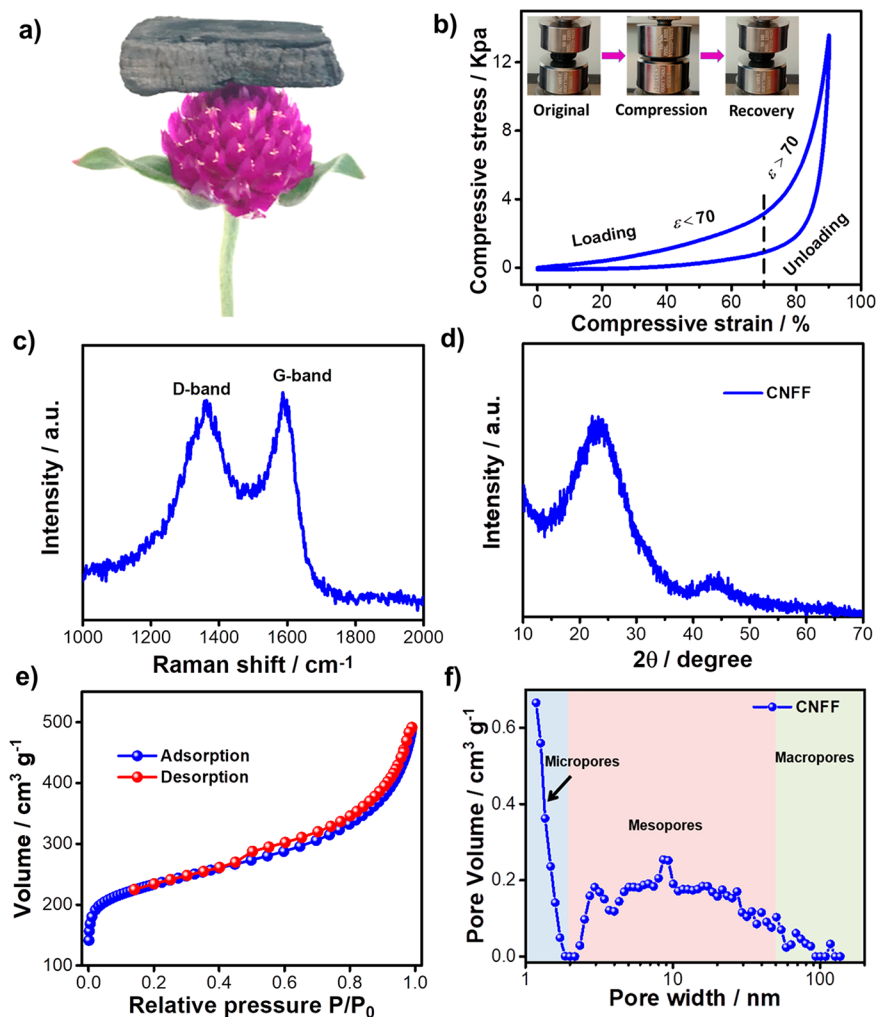
Figure 2. (a) Photograph of the CNFF standing on a flower, indicating its foam-like property. (b) Compressive stress−strain curves of the loading−unloading cycle at a strain of 90% of the CNFF. The insets in panel b are the sequential photographs of the CNFF during the compression process. (c) Raman spectroscopy of CNFF. (d) XRD pattern of CNFF. (e) Representative nitrogen adsorption−desorption isotherm curve of CNFF. (f) Pore size distribution of the CNFF electrode.

structure is the hierarchical porous structure, which contains micropores on the carbon nanofiber as well as micro- and mesopores between the fibers, which provides plenty of effective sites for potassium ion storage. Another important feature of the CNFF is that the 3D carbon foam is highly conductive, allowing electron transportation, and the free space in the 3D network provides sufficient pathways for electrolyte infiltration into the structure. Lastly, the quasi-amorphous carbon possesses large interlayer spacing within a short range, which has the capability to accommodate a large number of potassium ions during depotassiation and potassiation.[15] Based on the above advantages, in the rate-performance test, the CNFF electrode delivers high initial reversible capacities of 240 and 214 mA h g^{-1} at 50 and 100 mA g^{-1}, respectively. In the long-term cycling stability test, at a high current density of 1000 mA g^{-1}, the CNFF electrode maintains a stable capacity of 158 mA h g^{-1} for 2000 cycles, which translates into an average capacity decay of 0.006% per cycle. After cycling at 1000 mA g^{-1} for 2000 cycles, the CNFF electrode is able to maintain a capacity of 141 mA h g^{-1} at a current density of 2000 mA g^{-1} for another 1500 cycles and a capacity of 122 mA h g^{-1} at a current density of 5000 mA g^{-1} for an additional 1000 cycles. Through the electrode reaction kinetic analysis, a

surface-induced capacitive process and diffusion-controlled process were proposed to be the mechanism for the charge storage. The 3D porous carbon foam derived from BC is beneficial to enhancing the surface area, electrolyte transport, and charge storage.[24] This work will open new opportunities for developing high-performance and cost-effective energy storage materials from sustainable biomaterials.

Results and Discussion. Transmission electron microscopy (TEM) and scanning electron microscopy (SEM) were employed to inspect the morphology of BC aerogel and CNFF. BC is a homopolysaccharide with a high molecular weight, with each molecule consisting of β-1,4 linked anhydro-D-glucopyranose units (Figure S1a). BC can be generated by a cost-effective *Acetobacter xylinum* large-scale fermentation process (Figures 1a and S1b). Figures 1b and S2 are SEM images of BC aerogel. The large piece of BC hydrogel was cut into rectangular shape pellicles (Figure 1c) followed by freeze-drying process to obtain the BC aerogel. The CNFF was then obtained by pyrolysis of BC aerogel at 1000 °C under N_2 atmosphere. The CNFF product exhibits a hierarchical porous and 3D nanofibrillar reticulated structure (Figure 1d). After the carbonization treatment, a high-magnification SEM image is used to indicate that the porous 3D network structure of the
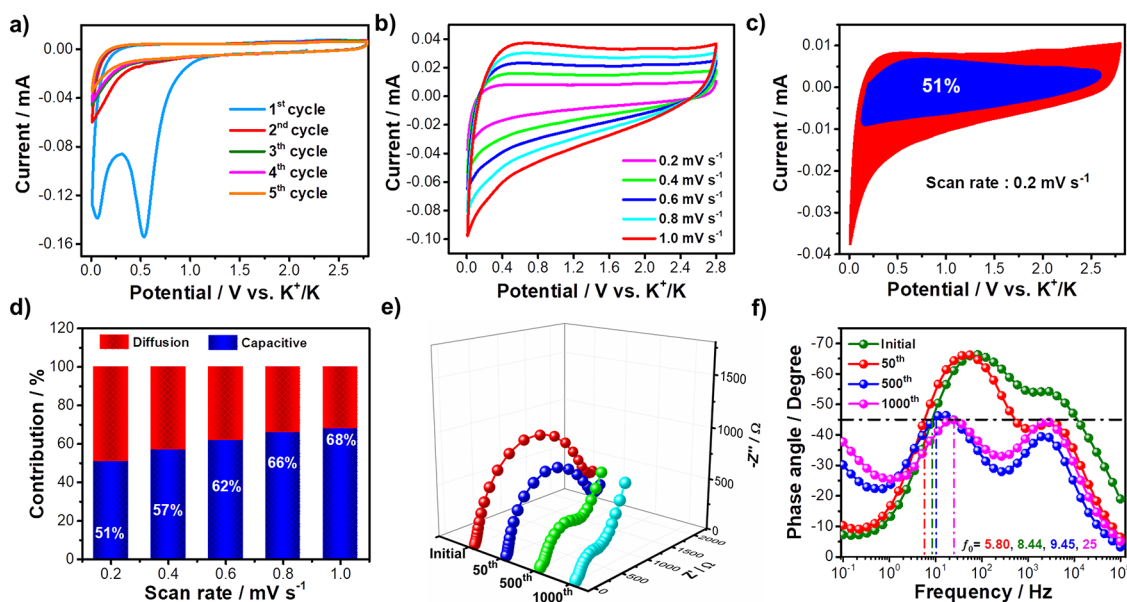
Figure 3. Electrochemical kinetic analysis of potassium ions storage behavior of CNFF electrodes. (a) CV curves (first to fifth cycles) obtained at the scan rate of 0.1 mV s^{-1}. (b) CV curves obtained at the scan rates of 0.2, 0.4, 0.6, 0.8, and 1.0 mV s^{-1}. (c) Capacitive charge-storage contributions at scan rates of 0.2 mV s^{-1}. (d) Contribution ratios of capacitive and diffusion capacities at various scan rates. (e) Nyquist plots of CNFF anode after different cycles. The equivalent circuit model is shown in Figure S10. (f) Bode plot of CNFF anode.

BC aerogel is maintained, along with large numbers of junctions and nanofibers with a diameter between 10 and 30 nm (Figure 1e). Hierarchical pores, necessary for trapping potassium ions, were generated between the fibers when the CNFF was compressed in the battery (Figure 1f). The TEM image of CNFF (Figure 1g) further confirms the fibrous structure, which could enable fast electron and ion transport along 3D directions. The TEM image of higher magnification (Figures 1h and S3) shows lots of nanopores on the surface of the carbonized nanofibers, which are beneficial for absorbing the potassium ions. The first level pore is micropores on the carbon nanofiber (Figure S3a–c). The second level pore is micro- and mesopores between the fibers (Figure S3d–f). High-resolution TEM (HRTEM) image reveals a disordered pattern with localized short-range order (Figures 1i and S4). The interlayer spacing of d_{002} was measured to be 0.38 ± 0.01 nm, which is larger than that of graphite (0.34 nm). The large interlayer spacing implies a potential to accommodate a certain amount of potassium ions during depotassiation and potassiation. The high-angle annular dark-field scanning TEM and elemental mapping images clearly reveal the distributions of C in the CNFF (Figure S5).

Stress−strain curves, X-ray diffraction (XRD), N_2 adsorption−desorption isotherms, and Raman spectra were used to further investigate the structure and composition of CNFF. A piece of CNFF with dimensions of 2.4 cm × 1.3 cm × 0.6 cm (length × width × height) weighs 9.96 mg (Figure S6a,b). Thus, it can stand on the top of a flower stably (Figure 2a). It is noteworthy that the CNFF is fire resistant when exposed to the flames from ethanol. No volume shrinkage of CNFF is observed after repeated exposures to flames, and its morphology and inherent 3D porous structure remain the same (Figure S7). Mechanically, CNFF is highly elastic and flexible. As shown in Figure 2b, CNFF can withstand a manual compression of up to 90% volume reduction and still recover its original volume without any fractures, proving that the material is elastic and robust. In the stress−strain curve, two

characteristic regions can be recognized in the loading process (ε_{maxima} = 90%) a linear elastic region of ε < 70% due to the bending of nanofibers and the elastic buckling of nanofibrous pores, and a densification region of ε > 70% due to complete collapse. The stresses remain above 0 until ε = 0 in the unloading process, suggesting complete volume recovery without deformations. When the CNFF is compressed to a 90% volume reduction, it has a very low compressive stress of 13.8 KPa owing to its highly porous and compressible structure. Figure 2c displays the Raman spectroscopy analysis for CNFF, which exhibits the two peaks at 1361 and 1591 cm^{-1} assigned to the D band and the G band of carbon, respectively. The degree of graphitic disordering I_D/I_G is 0.85 for CNFF. The obviously broadened diffraction (002) peak in the XRD pattern at 2θ = 23.59° is shown in Figure 2d. According to the Bragg's law, the interlayer spacing of CNFF is ∼0.38 nm, which is the same with HR-TEM analysis. The specific surface area and pore size distribution of the CNFF were further investigated by nitrogen adsorption−desorption isotherms. The isotherm curve exhibits an obvious volume jump at very low relative pressure due to micropores filling, and the pronounced hysteresis loop reveals the majority of mesopores (Figure 2e). Based on the BET test, the CNFF possesses a high specific surface area of 778.75 m^2 g^{-1}. The peaks for the micropores and mesopores dominate the chart of pore size distribution, with the micropores accounting for 53.32% of the total surface area, as shown in Figure 2f. The percolated 3D network structures and the large amount of the micropores inside CNFF facilitate the rapid transport of electrons and ions, which is significant for the storage of potassium ions in the PIBs. Meanwhile, the cost analysis of the CNFF electrode with commercial carbon foam and graphene foam are presented in Table S1.

In Figure 3, the detailed electrochemical characteristics of the CNFF were presented. Typically, cyclic voltammetry (CV) analysis is applied to get a deep understanding into unique surface-driven dominated potassium ion storage behavior.
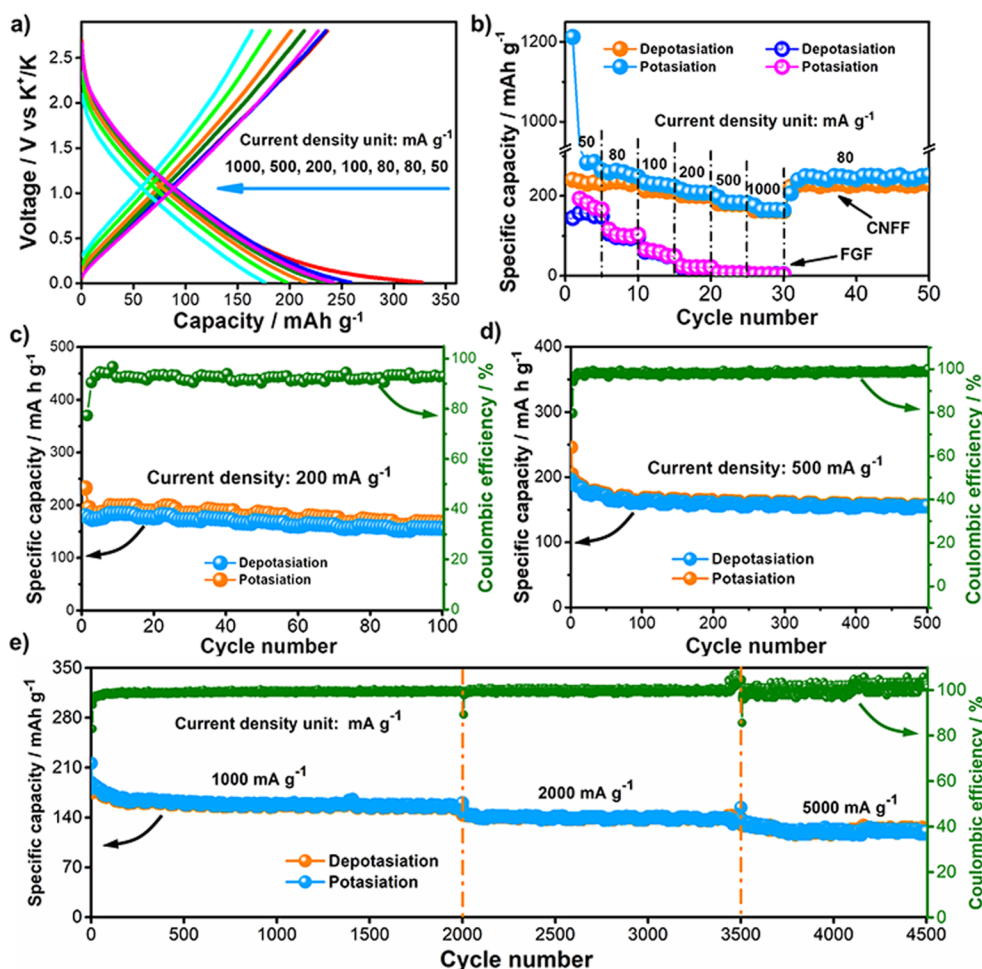
Figure 4. (a) Depotassiation-potassiation profiles of CNFF at various current densities. (b) Rate capability of CNFF and free-standing graphene film at current densities from 50 to 1000 mA g^{-1} for PIB. (c) Cycling performances of CNFF at current density of 200 mA g^{-1}. (d) Cycling performances of CNFF at current density of 500 mA g^{-1}. (e) Long-term cycling performances of CNFF anode at different current densities of 1000, 2000, and 5000 mA g^{-1}. The battery rested for 10 days before the current density changed.

Figure 3a shows the CV curves of the CNFF/potassium half-cells in the voltage range of 0.01−2.80 V (versus K$^+$/K) at a scan rate of 0.1 mV s^{-1}. The broad reduction peak below 1.0 V on the first cycle is due to the formation of solid electrolyte interphase (SEI) film on the CNFF electrode.[25] Furthermore, the CV curves from the second cycle to the fifth cycle are very comparable, indicating excellent reversibility.

Moreover, according to the following Equation 1, two kinds of charge storage mechanism of the capacitive effects (k_1v) and diffusion-controlled ($k_2v^{1/2}$) contributions can be identified by CV curve analysis (Figure 3b):[3,26]

$$i(V) = k_1v + k_2v^{1/2} \tag{1}$$

or

$$i(V)/v^{1/2} = k_1v^{1/2} + k_2 \tag{2}$$

where k_1 and k_2 are constants, i is the current (A) at a fixed potential, and v is the sweep rate (mV s^{-1}). According to eq 2, as shown in Figure S8, the slope obtained by fitting the line represents k_1, and the resulting intercept represents k_2. Figures 3c and S9 show the CV curves analysis at various sweep rates from 0.2 to 1.0 mV s^{-1}. Among the CV curves, the capacitive-controlled region marked as blue and the diffusion-controlled region marked as red. The capacitive-controlled contribution is

51% at a low scan rate of 0.2 mV s^{-1}. The proportions of capacitive contribution increased gradually with the sweep rate and reached up to 68% at a high scan rate of 1.0 mV s^{-1} (Figure 3d). This phenomenon further confirmed that the capacitive- and diffusion-controlled are two potassium ion storage mechanisms in CNFF.[27] The adsorption of the potassium ions on the CNFF electrode, caused by the large specific area and rich ion trapping pores. Meanwhile, the steady contribution of the adsorptive mechanism (double-layer capacitance effect) significantly enhances the overall capacity of CNFF-based PIBs.

To evaluate the charge-transfer resistance and ion diffusion of CNFF electrode after the initial, 50th, 500th, and 1000th cycles, the electrochemical impedance spectroscopy (EIS) analysis was employed. As shown in Figure 3e, two regions are defined at the Nyquist plots: (1) the semicircle in the high-frequency to medium-frequency region and (2) the Warburg line in the low-frequency region. The semicircle represents the charge-transfer resistance (R_{ct}), and the sloping line corresponds to the ion diffusion.[28] It can be found that the R_{ct} continuously decreases from 2037 Ω for the initial cycle to 1531 Ω for the 50th cycle and continues to decrease to 55 and 46 Ω for the 500th and 1000th cycles, respectively (Table S2). It suggests that both the charge-transfer resistance and the ion

diffusion resistance of CNFF anode are reduced after cycling. This unique behavior can be explained as the "self-activating" process.[28] The bode plot between the phase angles and the frequencies of PIBs are shown in Figure 3f. The characteristic frequency f_0 ($-45°$ phase angle) increases from 5.8 Hz (Initial) to 25 Hz (1000th cycle). Therefore, the corresponding relaxation time constant τ_0, which was derived from reciprocal of frequency, is largely shortened from 0.17 s (Initial) to 0.04 s (1000th cycle), suggesting the accelerating electrochemical response.

The CNFF was tested as an anode material in half cells to illustrate its potential for PIBs. Due to its unique structure and high electronic conductivity, foam was used directly as the working anode without a current collector, conductive additive, and binder. The rate capability of the CNFF electrode is described in Figure 4a,b. The reversible capacity of the electrode was 240, 236, 214, 202, 181, and 164 mAh g^{-1} at the current density of 50, 80, 100, 200, 500, and 1000 mA g^{-1}, respectively. More importantly, after cycling at high current densities, the electrode was able to maintain a reversible capacity of 230 mAh g^{-1} at a lower current density of 80 mA g^{-1}. The initial depotassiation and potassiation curves are displayed separately in Figure S11, from which we can see CNFF with high initial capacity shows a large irreversible capacity associated with SEI formation in the first cycle, indicating that the electrochemical behavior of CNFF is strongly related to electrode's high surface area.[25] In the future, we will use different approaches to further improve the first Coulombic efficiency, including conducting pre-potassiation of electrode, constructing composite electrode, and reducing the specific surface area of the electrode. After the first cycle, no obvious plateau is observed during the depotassiation–potassiation cycle. The loss of reaction plateau can be explained by two possible reasons. One reason is that a large number of potassium ions experience adsorption and desorption on the micro- and mesopores of CNFF, leading to the inconspicuous voltage plateau. The other reason is that the larger size of potassium ions could cause sluggish kinetics of the chemical reaction.[27] When compared to the rate performance of freestanding graphene film (FGF)-based PIB anodes, the rate capability of CNFF-based PIBs has a much higher at various current densities. Although a capacity of 148 mAh g^{-1} is achieved for FGF-based PIB under the current density of 50 mA g^{-1}, the capacity decays rapidly with the increase of current density. There is no capacity contribution from FGF after current density of 200 mA g^{-1} (Figure 4b). This means that the very limited interlayer spacing and very limited pore structure of FGF cannot potassiate or depotassiate.[29] Upon the various current density, the outstanding cycling capability of CNFF further proves its remarkable reversibility and stability. After 100 cycles at a current density of 200 mA g^{-1}, the depotassiation capacity remains 168 mAh g^{-1} (Figure 4c). When the current density is further increased to 500 mA g^{-1}, the capacity retention is 156 mAh g^{-1} after 500 cycles (Figure 4d). After the above cycling, the battery was left alone for 10 days and then was tested at a current density of 500 mA g^{-1}. It can be seen that the performance of same battery still achieves a capacity of 143 mAh g^{-1} after another 500 cycles (Figure S12). In addition, the batteries were also worked at the current density of 1000 mA g^{-1} for 2000 cycles to test the long-term cycling stability. From the Figure 4e, it can be clearly seen that a reversible capacity of 158 mAh g^{-1} is obtained upon cycling, which has an average capacity decay of

0.006% per cycle. After the first 2000 cycles at 1000 mA g^{-1} finished, the battery was tested under the high current densities of 2000 mA g^{-1} for 1500 cycles and 5000 mA g^{-1} for 1000 cycles, respectively. The capacity of CNFF electrode reachs to 141 mAh g^{-1} at 2000 mA g^{-1} after 1500 cycles and 122 mAh g^{-1} after another 1000 cycles at 5000 mA g^{-1}, respectively.

The electrochemical performance of CNFF-based PIBs is more attractive than most of the state-of-art of carbon and metal material-based PIB anodes (compared in Table S3). From the above experimental results, a large number of pore structures and the fibrous structure present the synergistic effect for boosting the electrochemical performance. The superior performance is attributed to the following reasons. First, the micropores, which account for more than 50% of the total surface area on the carbon nanofiber, can act as reservoirs for the storage of potassium ions. Second, under the compression of 1D nanofibers, the large amount of micro- and mesopores between the nanofibers can also store potassium ions. The PIB half-cell is able to lighten a red light-emitting diode (working voltage of 1.9–2.2 V; Figure S13) after being fully charged. Figure S14 shows SEM images (side view and top view) after the battery was cycled 1000 times at a current density of 500 mA g^{-1}, from which we can see that the structure of carbon nanofiber is preserved and contains a large number of pore structures. These images evidence that the structure of carbon electrode is well-maintained under compression, which is crucial for electron transport and battery cycling stability. Hence, the compressibility of CNFF is a critical factor for cycling stability.

Conclusions. In conclusion, a compressible, hierarchical porous, and high-performance BC-derived CNFF was developed in an economical and eco-friendly way as the free-standing anode of PIBs. Electrochemical tests showed that the CNFF-based PIBs exhibit a high stable capacity of 240 mAh g^{-1} at current density of 50 mA g^{-1} and a capacity of 122 mAh g^{-1} at high current density of 5000 mA g^{-1}. Meanwhile, for the cycling performances, the battery at current density of 1000 mA g^{-1} maintains a highly reversible capacity of 158 mAh g^{-1} for more than 2000 cycles with only 0.006% capacity decay per cycle. This performance is superior to most carbon-based electrodes currently in PIBs. The high reversible capacity and excellent cycle capability can be attributed to three main reasons. The first is the hierarchical pores of the structure. The micropores on carbon nanofiber and the micro- and mesopores between the fibers provide an abundance of effective sites for potassium ion storage. The second reason is that the 3D carbon foam not only provides a highly conductive reticulated network for electron transport but also supplies sufficient space for the transportation of electrolyte through the porous structure, which promoted the outstanding rate performance. The third and final reason is that the quasi-amorphous carbon possesses larger interlayer spacing in a shorter range compared to graphite, indicating the potential to accommodate a certain amount of potassium ions during charge and discharge. This work will encourage further research for cost-effective and eco-friendly materials used for PIBs and other electrochemical energy-storage systems.

■ ASSOCIATED CONTENT

ⓈSupporting Information

The Supporting Information is available free of charge on the ACS Publications website at DOI: 10.1021/acs.nanolett.8b03845.

Additional experimental details; figures including chemical structures, BC pellicles, microscopy results, experimental materials and procedures, cycling performance, charge-storage contributions, and circuit models; tables showing cost analysis, EIS characteristics, and a comparison of experimental performance results (PDF)

AUTHOR INFORMATION

Corresponding Author

*E-mail: h.zhu@neu.edu.

ORCID ⓘ

Hongyan Li: 0000-0002-7073-5198

Hongli Zhu: 0000-0003-1733-4333

Author Contributions

#H. L. and Z. C. contributed equally to this work.

Notes

The authors declare no competing financial interest.

REFERENCES

(1) Zhao, J.; Zhou, G.; Yan, K.; Xie, J.; Li, Y.; Liao, L.; Jin, Y.; Liu, K.; Hsu, P. C.; Wang, J.; et al. *Nat. Nanotechnol.* **2017**, *12* (10), 993–999.

(2) Olivetti, E. A.; Ceder, G.; Gaustad, G. G.; Fu, X. *Joule* **2017**, *1*, 229–243.

(3) Xu, Y.; Zhang, C.; Zhou, M.; Fu, Q.; Zhao, C.; Wu, M.; Lei, Y. *Nat. Commun.* **2018**, *9*, 1720–1730.

(4) Chen, Y.; Luo, W.; Carter, M.; Zhou, L.; Dai, J.; Fu, K.; Lacey, S.; Li, T.; Wan, J.; Han, X.; et al. *Nano Energy* **2015**, *18*, 205–211.

(5) Luo, W.; Wan, J.; Ozdemir, B.; Bao, W.; Chen, Y.; Dai, J.; Lin, H.; Xu, Y.; Gu, F.; Barone, V.; Hu, L. *Nano Lett.* **2015**, *15*, 7671–7677.

(6) Jian, Z.; Luo, W.; Ji, X. *J. Am. Chem. Soc.* **2015**, *137*, 11566–11569.

(7) Jian, Z.; Xing, Z.; Bommier, C.; Li, Z.; Ji, X. *Adv. Energy Mater.* **2016**, *6*, 1501874.

(8) Lee, J. H.; Ali, G.; Kim, D. H.; Chung, K. Y. *Adv. Energy Mater.* **2017**, *7*, 1601491.

(9) Zeng, C.; Xie, F.; Yang, X.; Jaroniec, M.; Zhang, L.; Qiao, S. Z. *Angew. Chem., Int. Ed.* **2018**, *57*, 8540–8544.

(10) Zhang, W.; Mao, J.; Li, S.; Chen, Z.; Guo, Z. *J. Am. Chem. Soc.* **2017**, *139*, 3316–3319.

(11) Chen, C.; Wang, Z.; Zhang, B.; Miao, L.; Cai, J.; Peng, L.; Huang, Y.; Jiang, J.; Huang, Y.; Zhang, L.; et al. *Energy Storage Materials* **2017**, *8*, 161–168.

(12) Ren, X.; Zhao, Q.; McCulloch, W. D.; Wu, Y. *Nano Res.* **2017**, *10*, 1313–1321.

(13) Yang, C.; Feng, J.; Lv, F.; Zhou, J.; Lin, C.; Wang, K.; Zhang, Y.; Yang, Y.; Wang, W.; Li, J.; et al. *Adv. Mater.* **2018**, *30*, 1800036.

(14) Li, D.; Zhu, M.; Chen, L.; Chen, L.; Zhai, W.; Ai, Q.; Hou, G.; Sun, Q.; Liu, Y.; Liang, Z.; et al. *Adv. Mater. Interfaces* **2018**, *5*, 1800606.

(15) Chen, M.; Wang, W.; Liang, X.; Gong, S.; Liu, J.; Wang, Q.; Guo, S.; Yang, H. *Adv. Energy Mater.* **2018**, *8*, 1800171.

(16) Wei, Z.; Wang, D.; Li, M.; Gao, Y.; Wang, C.; Chen, G.; Du, F. *Adv. Energy Mater.* **2018**, *8*, 1801102.

(17) Wu, Z. Y.; Liang, H. W.; Chen, L. F.; Hu, B. C.; Yu, S. H. *Acc. Chem. Res.* **2016**, *49*, 96–105.

(18) Vasconcelos, N. F.; Feitosa, J. P. A.; da Gama, F. M. P.; Morais, J. P. S.; Andrade, F. K.; de Souza Filho, M. d. S. M.; de Freitas Rosa, M. *Carbohydr. Polym.* **2017**, *155*, 425–431.

(19) Shen, X.; Shamshina, J. L.; Berton, P.; Gurau, G.; Rogers, R. D. *Green Chem.* **2016**, *18*, 53–75.

(20) Cheng, Z.; Yang, R.; Liu, X.; Liu, X.; Chen, H. *Bioresour. Technol.* **2017**, *234*, 8–14.

(21) Håkansson, K. M.; Fall, A. B.; Lundell, F.; Yu, S.; Krywka, C.; Roth, S. V.; Santoro, G.; Kvick, M.; Wittberg, L. P.; Wågberg, L.; et al. *Nat. Commun.* **2014**, *5*, 4018.

(22) Wang, S.; Jiang, F.; Xu, X.; Kuang, Y.; Fu, K.; Hitz, E.; Hu, L. *Adv. Mater.* **2017**, *29*, 1702498.

(23) Liang, H. W.; Guan, Q. F.; Song, L. T.; Yao, H. B.; Lei, X.; Yu, S. H.; Zhu, Z. *NPG Asia Mater.* **2012**, *4* (6), e19.

(24) Wu, Z. Y.; Liang, H. W.; Hu, B. C.; Yu, S. H. *Angew. Chem.* **2018**, DOI: 10.1002/ange.201802663.

(25) Wang, Y.; Wang, Z.; Chen, Y.; Zhang, H.; Yousaf, M.; Wu, H.; Zou, M.; Cao, A.; Han, R. P. *Adv. Mater.* **2018**, *30*, 1802074.

(26) Brezesinski, T.; Wang, J.; Tolbert, S. H.; Dunn, B. *Nat. Mater.* **2010**, *9* (2), 146–151.

(27) Wang, W.; Zhou, J.; Wang, Z.; Zhao, L.; Li, P.; Yang, Y.; Yang, C.; Huang, H.; Guo, S. *Adv. Energy Mater.* **2018**, *8*, 1701648.

(28) Wang, G.; Yu, M.; Wang, J.; Li, D.; Tan, D.; Löffler, M.; Zhuang, X.; Müllen, K.; Feng, X. *Adv. Mater.* **2018**, *30*, 1800533.

(29) Bin, D. S.; Lin, X. J.; Sun, Y. G.; Xu, Y. S.; Zhang, K.; Cao, A. M.; Wan, L. *J. Am. Chem. Soc.* **2018**, *140*, 7127–7134.